# High efficiency radio frequency antennas for amplifier free quantum sensing applications

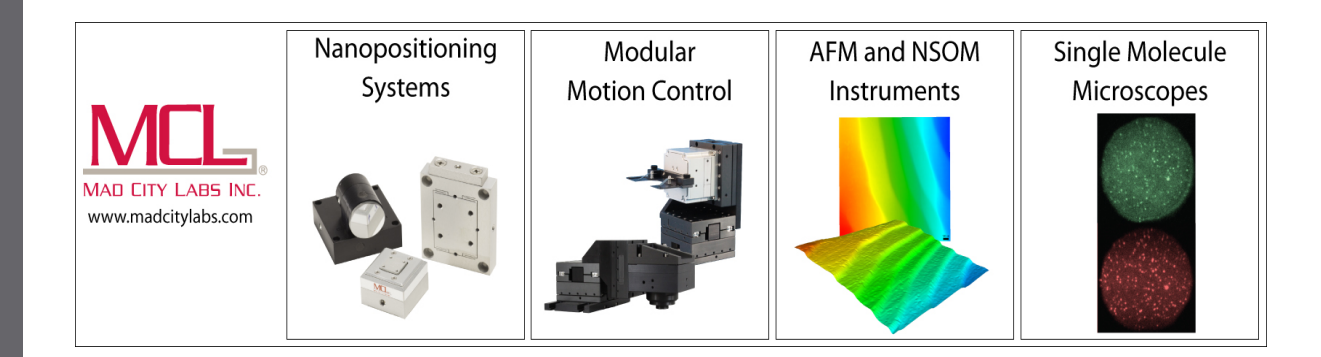
Cite as: Rev. Sci. Instrum. **94**, 044701 (2023); https://doi.org/10.1063/5.0136233 Submitted: 29 November 2022 • Accepted: 14 March 2023 • Published Online: 03 April 2023













# High efficiency radio frequency antennas for amplifier free quantum sensing applications

Cite as: Rev. Sci. Instrum. 94, 044701 (2023); doi: 10.1063/5.0136233 Submitted: 29 November 2022 • Accepted: 14 March 2023 •









Published Online: 3 April 2023







## **AFFILIATIONS**

- Department of Physics and Engineering Physics, Morgan State University, Baltimore, Maryland 21234, USA
- <sup>2</sup> Department of Electrical and Computer Engineering, Morgan State University, Baltimore, Maryland 21234, USA
- Department of Electrical and Computer Engineering, Cornell University, Ithaca, New York 14850, USA

#### **ABSTRACT**

Radio frequency (RF) signals are frequently used in emerging quantum applications due to their spin state manipulation capability. Efficient coupling of RF signals into a particular quantum system requires the utilization of carefully designed and fabricated antennas. Nitrogen vacancy (NV) defects in diamond are commonly utilized platforms in quantum sensing experiments with the optically detected magnetic resonance (ODMR) method, where an RF antenna is an essential element. We report on the design and fabrication of high efficiency coplanar RF antennas for quantum sensing applications. Single and double ring coplanar RF antennas were designed with -37 dB experimental return loss at 2.87 GHz, the zero-field splitting frequency of the negatively charged NV defect in diamond. The efficiency of both antennas was demonstrated in magnetic field sensing experiments with NV color centers in diamond. An RF amplifier was not needed, and the 0 dB output of a standard RF signal generator was adequate to run the ODMR experiments due to the high efficiency of the RF

Published under an exclusive license by AIP Publishing. https://doi.org/10.1063/5.0136233

#### I. INTRODUCTION

Research on contemporary quantum applications in computing, telecommunication, and sensing is currently growing at an exponential rate.<sup>1-4</sup> Radio frequency (RF) signals are commonly used for the manipulation of spins in most of these applications. Among various quantum sensing approaches, solid state defects were demonstrated in the detection of extremely small changes in physical quantities, such as temperature, pressure, electric, and magnetic fields. 5-8 Nitrogen vacancy (NV) defects in diamond are widely studied owing to their room temperature operation capability and millisecond long spin coherence times  $(T_2)$ . Point defects in other wide bandgap semiconductors, including silicon carbide (SiC) and hexagonal boron nitride (hBN), were also utilized in quantum sensing experiments.<sup>2,5</sup> Optically detected magnetic resonance (ODMR) method is a key component in this solid-state defect based quantum sensing approach, where RF antennas are crucial for the application of microwave signals to the samples. In the ODMR method, spin manipulation associated with a defect is achieved through the application of its characteristic zero-field splitting (ZFS) frequency signal. Thus, high efficiency and frequency tunable RF antennas are

critical for the successful implementation of solid-state defect-based quantum sensing experiments.

The high efficiency of microwave radiation performance of an antenna depends on parameters, such as resonance frequency, field radiation pattern, and impedance matching. There are established techniques to design antennas with desired operation frequencies and radiation losses. RF antennas with different geometries and materials were previously utilized in quantum sensing experiments. In the simplest case, one end of an RF cable can be stripped to form a loop antenna. Copper and gold wire antennas were shown to be effective. 10,11 These antennas are easy to design and fabricate, but they do not generate a uniform magnetic field, and their energy loss is comparatively high, requiring the use of RF amplifiers to compensate for energy losses by applying high power microwaves. Coplanar and microstrip printed circuit board (PCB) RF antennas are also commonly used in ODMR experiments. 12-14 Compared with wire antennas, PCB antennas provide a large area uniform magnetic field pattern and higher return losses, making them more efficient for quantum sensing applications. 15 Efficient coplanar RF antennas are also needed in other engineering applications, such as Wireless Local Area Network (WLAN) (2.4/5.2/5.8 GHz) and Worldwide

a) Author to whom correspondence should be addressed: birol.ozturk@morgan.edu

Interoperability for Microwave Access (WiMAX) (2.3/2.5/5.5 GHz) bands. 16-19

Microstrip PCB antennas with a maximum of -23.5 dB return loss were demonstrated, <sup>20</sup> but RF amplifiers were still needed in ODMR experiments with these antennas. Removal of the need for an RF amplifier is an important size reduction step for diamond magnetometry setups as this will also remove the need for the RF amplifier power supply. Although benchtop NV diamond quantum magnetometry is demonstrated in numerous research laboratories globally, and there are currently several companies selling tabletop NV diamond magnetometers, a handheld device for field operation is yet to be demonstrated. To this end, the elimination and size reduction of components in these bulky benchtop setups is a critical task for the realization of many real-life applications.

Here, we report on the design, fabrication, and characterization of high efficiency single and double ring coplanar RF antennas for quantum sensing experiments with NV color defects in diamond. Our RF antennas remarkably exhibited up to -37 dB experimental S11 return loss and uniform large area magnetic field generation. Antennas were tested in ODMR experiments for quantum sensing of magnetic fields with NV defects in diamond, where an RF amplifier was not needed due to high efficiencies of the antennas. We have also demonstrated the tunability of antenna resonant frequency, facilitating their use in quantum sensing experiments with other defects in wide bandgap semiconductors, such as silicon carbide (SiC) and cubic boron nitride (cBN). <sup>2,21,22</sup>

# II. DESIGN AND FABRICATION OF RF ANTENNAS

Antenna substrate material selection is critical for reproducible and high efficiency RF antenna design and fabrication. The substrate's thickness and dielectric constant impact the antenna performance as well as the size of the antenna. In this work, Isola (IS-680-280) and Rogers (4003) brand PCB substrates were used in antenna fabrication, where both substrates have high purity copper cladding of 0.035 mm thickness. Table I summarizes the properties of both substrates. Isola and Rogers substrates were chosen as their properties are readily available in the material libraries of common simulations tools such as Computer Simulation Technology (CST) Microwave studio and Ansys HFSS, facilitating the achievement of reliable antenna performance after fabrication. Furthermore, these substrates have very low loss tangent, which is also known by dissipation factor compared with typical high values of more commonly utilized FR-4 (0.02-0.03) antenna substrate material. This dissipation factor generally refers to the inherent transmission losses through the material.

Ansys HFSS software was employed for the design and optimization of the RF antenna parameters. A single ring coplanar RF

antenna was designed for the Isola-680-280 substrate. The single ring antenna offers several significant advantages. First, its simple structure makes it both easy to fabricate and inexpensive, making it an attractive option for many applications. Second, it can be seamlessly integrated with other components on a printed circuit board (PCB) and efficiently matched to a transmission line for effective power transfer. Furthermore, the single ring coplanar antenna boasts a broad bandwidth and high radiation efficiency, resulting in a significant amount of power being radiated with minimal loss. This makes it a suitable choice for a wide range of wireless communication systems and ODMR operations. Figure 1(a) shows the diagram of the single ring antenna design and associated geometric parameters are listed in Table II. This antenna consists of a single radiating copper ring and the SMA (SubMiniature version A) feedline. The single ring is 27.5 mm in size with a width of 4 mm (c = e) and a split gap size of d = 2 mm. As a coplanar antenna, it is surrounded by a ground plane where L = 38, W = 40, and f = 5 mm. The feedline connection for the antenna is 6.25 mm in length (h) and 1 mm in width. Multiple air holes were placed in between the ground and the radiating single ring planes of the antenna to avoid background emission from the substrate while using the fabricated antenna. As shown in Fig. 1(c), the simulated return loss (S11) for this antenna was -36 dB.

We designed a second coplanar RF antenna for the Rogers-4003 substrate, which has a 3.55 dielectric constant and a thickness of 0.508 mm. This antenna has two split rings surrounded by a ground plane [Fig. 1(c)]. The single innermost ring of this antenna serves multiple purposes. First, it is designed to match the antenna's resonant frequency of 2.87 GHz, specifically for negatively charged NV diamond defects. Additionally, the innermost ring creates an additional gap, which is optimal for conducting ODMR experiments. In a coplanar antenna, magnetic fields are concentrated between the gaps of two rings, making these areas ideal for ODMR observations. By adding an extra inner ring, the antenna's magnetic field is further enhanced, creating more space to conduct ODMR experiments. To expand on this even further, the addition of more rings would create even more gaps, providing an even greater area for conducting ODMR experiments.

The optimized dimensions of the radiating outer ring were  $28 \times 28 \text{ mm}^2$  with a top split gap of 2 mm. The corners of the outer ring are truncated by 2 mm. The ground plane dimensions are  $38 \times 40 \text{ mm}^2$  and the feedline is in contact with the outer split wring as shown in Fig. 1(c). The inner split ring dimensions are  $16.62 \times 16.62 \text{ mm}^2$  with also a 2 mm gap, where the corners are truncated by 1.2 mm. All the optimized design parameters for the double ring antenna are shown in Table III. As depicted in Fig. 1(d), the simulated S11 for the double ring antenna was -37 dB at 2.87 GHz with the optimized parameters.

TABLE I. Properties of substrates used in the antenna fabrication.

Substrate material	Dielectric constant	Loss tangent (tan δ)	Thickness (mm)	Frequency range	Thermal stability (°C)	
Isola IS-680-280	2.80	0.0025-0.0035	0.80	Up to 110 GHz	55–125	
Rogers-4003	3.38	0.0027-0.0021	0.508	Up to 10 GHz	–55 to 288	

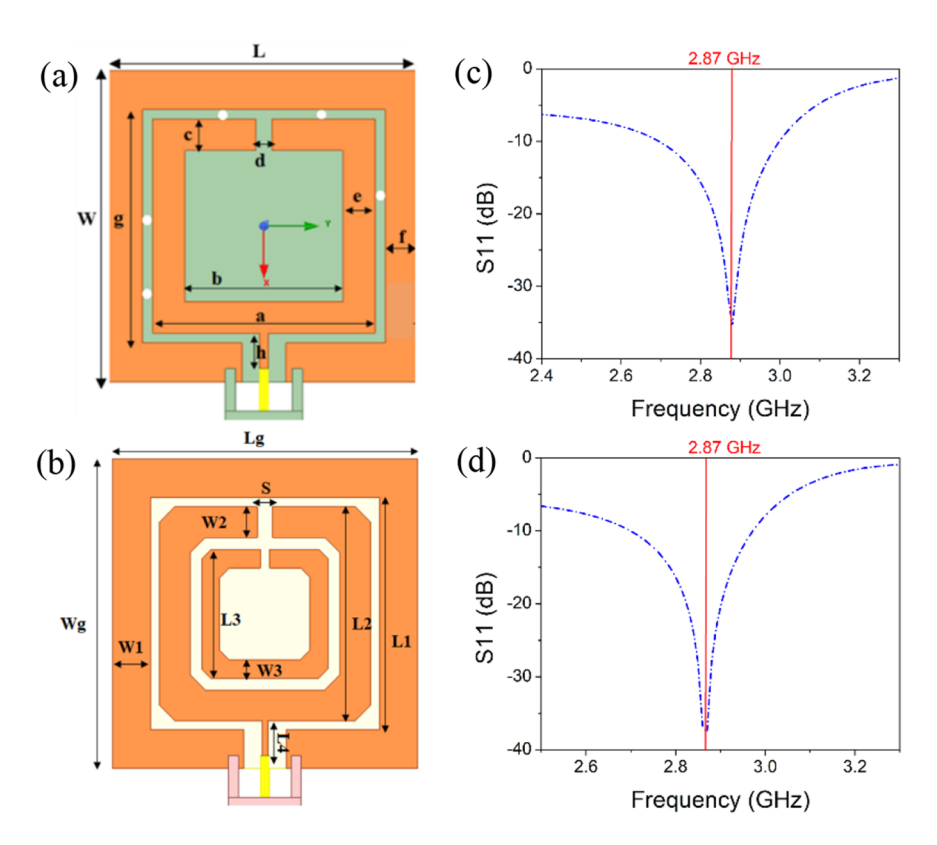


**FIG. 1.** (a) Single and (b) double ring RF antenna designs with geometric parameters. Simulated return losses (S11) of the (c) single and (d) double ring antennas.

TABLE II. Design parameters for Isola-680-280 substrate single split ring antenna.

Parameter	L	W	g	a	b	c = e	d	f	g	h	$R^a$
Value (mm)	38	40	30	27.5	20	4	2	4	30	6.25	0.6

<sup>&</sup>lt;sup>a</sup>R is the radius of the holes in between the single ring and ground planes.

TABLE III. Design parameters for Rogers-4003 substrate double split ring antenna.

Parameter	Lg	Wg	L1	W1	W2	L2	W3	L3	L4	S
Value (mm)	38	40	30	5	4	28	2.4	16.8	6	2

Antennas were photolithographically fabricated with simulated design parameters. We prepared photolithographic masks with the AutoCAD software according to optimized simulated design parameters. Masks were printed on a transparency by a commercial vendor (CAD/Art service) with high resolution (25000DPI). A positive photoresist (Microposit S1813 G2 positive) was spin coated on the substrates at 3000 RPM. A custom-built UV-exposure setup was used to transfer the pattern onto the photoresist using the printed masks. After developing, substrates were cleaned with deionized (DI) water and dried, followed by immersion into Ferric Chloride (FeCl<sub>3</sub>) etching solution. The remaining unexposed photoresist was removed with acetone. Coaxial female SMA connectors were soldered to the fabricated antennas as shown in the inset images in Fig. 2.

### **III. RESULTS AND DISCUSSIONS**

Return losses of antennas were characterized with a Vector Network Analyzer (LiteVNA). Figure 2 [panels (a) and (b)] shows simulated and experimental return loss (S11) graphs, where blue dashed and solid black lines represent simulated and fabricated antenna S11 results, respectively. Return losses of fabricated and simulated antennas were in good agreement. There were additional resonant frequency dips in the fabricated antennas at different frequencies, but they were not as pronounced. For both antennas, resonant frequency dips at 2.87 GHz were narrower compared with simulated dips at the same frequency.

After optimizing antenna parameters for a desired resonance frequency with computational simulations, certain dimensions such as the ring size can be varied to tune the resonant frequency of the antenna. This is necessary as the fabricated antenna may not exactly work at the desired resonant frequency due to fabrication errors or the effect of dielectric properties of the materials in the vicinity of the antenna such as the antenna holder and the sample being investigated. Designing and fabricating multiple antennas with a range of smaller and larger dimensions results in obtaining antennas that still operate highly efficiently at slightly different frequencies around

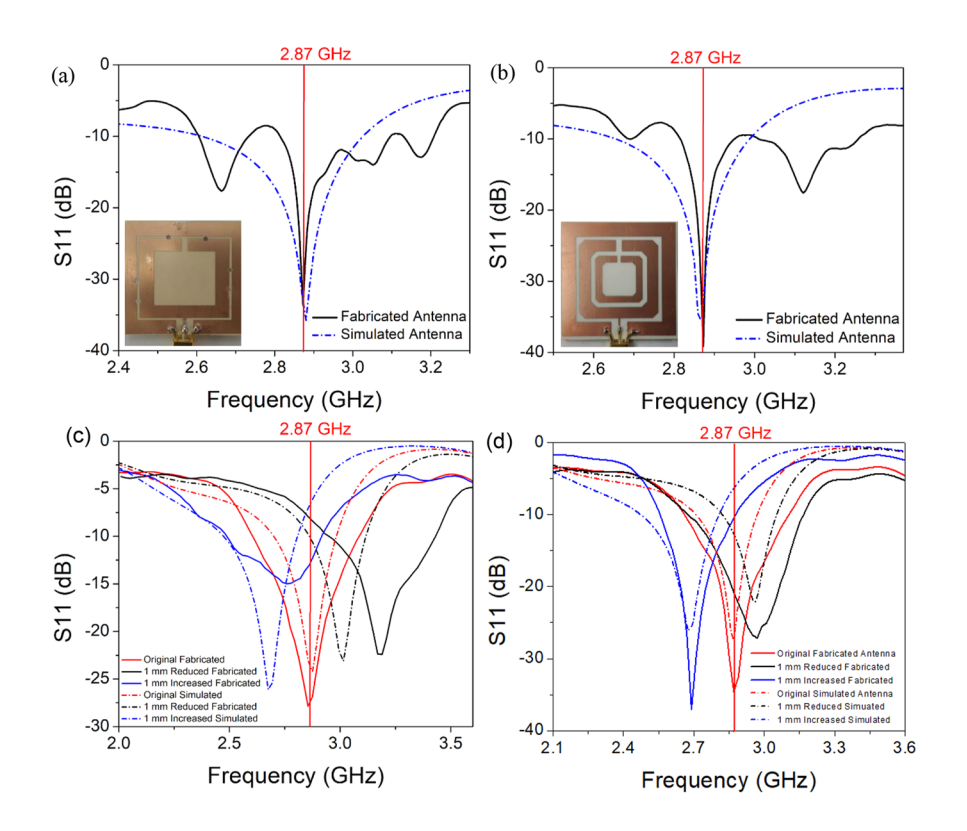


FIG. 2. Comparison of simulated and fabricated (a) single and (b) double ring antennas with the optimized parameters resulting in the highest return losses (S11). Demonstration of resonant frequency tuning with both simulated and fabricated (c) single and (d) double ring antennas.

the desired resonant frequency. For example, the optimized single ring antenna size (a parameter) is 27.5 mm for efficient radiation at 2.87 GHz but if we increase the size by 1 mm, the resonant frequency shifts to 2.72 GHz without significant loss in the S11 value as depicted with the dashed lines in Fig. 2(c). Conversely, when the size is reduced to 26.5 mm, the resonant frequency shifts to 3.01 GHz. The resonant frequency for the double ring antenna can also be tuned by changing the outer ring size. The optimized outer ring size (L2) is 28 mm for efficient performance at 2.87 GHz. The resonant frequency shifts to 2.69 GHz when the outer ring size is increased by 1 mm and it shifts to 2.96 GHz when the outer ring size is reduced to 27 mm as shown in Fig. 2(d) (dashed lines). Figure 2 [panels (c) and (d)] also shows the tunability of fabricated antenna resonant frequencies by changing the outer ring size. Mismatches between the exact values of resonant frequencies of simulated and fabricated antennas are caused by fabrication errors. Resonant frequency tuning simulations and fabrication were performed with slightly different geometrical parameters, where L and Lg dimensions were 40 mm instead of 38 mm, which causes slightly smaller simulated and fabricated return losses compared with highest efficiency antennas as shown in panels (c) and (d) in Fig. 2. In summary, the antenna ring size and the resonant frequency have an inverse relationship. The inductance increases with the increasing ring size, which shifts the resonance to lower frequencies. Inductance is reduced with the reduction in ring size, which increases the antenna's resonance frequency. This also leads to a change in capacitance as modifying only the ring size also affects the distance between ring and ground planes. Capacitance is inversely proportional to this gap

size by modeling ring and ground planes as parallel plate capacitor electrodes ( $c = \varepsilon A/d$ ). Increasing ring size reduces the gap size and increases the capacitance. The resonant frequency equation ( $f_r = 1/(2\pi\sqrt{LC})$ ) shows that the increase of inductance and capacitance decreases resonance frequency, which is caused by increasing antenna ring size.

We identified electromagnetic radiation patterns of the RF antennas with the electromagnetic simulations. As shown in the out-of-plane magnetic field (H) patterns in Fig. 3, the magnetic field is strongest between the ring and the ground plane for both antennas, and strong RF radiation in a large area is available for quantum sensing experiments. The maximum simulated magnetic field intensities were 133.4 A/m for single and 155.7 A/m for double ring antennas. Diamond samples with NV defects were placed in these areas for maximum radiation efficiency in the ODMR characterization experiments as explained below.

Fabricated antennas were tested in magnetic field quantum sensing experiments with the Optically Detected Magnetic Resonance (ODMR) method. A custom-built confocal photoluminescence setup was used in these experiments. A diagram of this setup is provided in the supplementary material document. A bulk diamond sample (Element Six DNV-B14) was placed on top of the antennas and in between ring and ground planes, where the magnetic field intensity is maximum based on simulation results. A 532 nm diode pumped solid-state (DPSS) laser was used for excitation of NV defects and high pressure (HP) Agilent 8648C RF signal generator was used to apply microwaves to the sample via fabricated RF antennas.

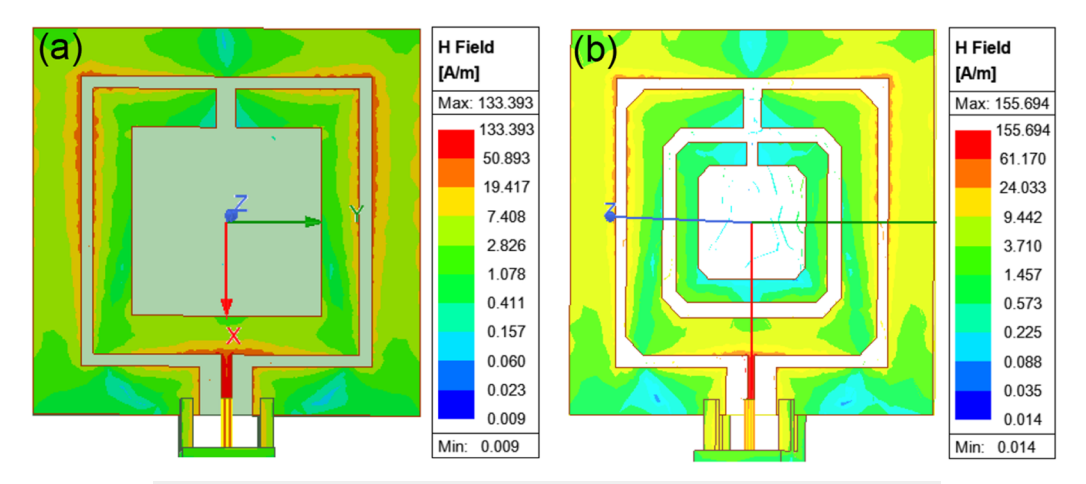


FIG. 3. Simulated out-of-plane magnetic field patterns of the (a) single and (b) double ring antennas.

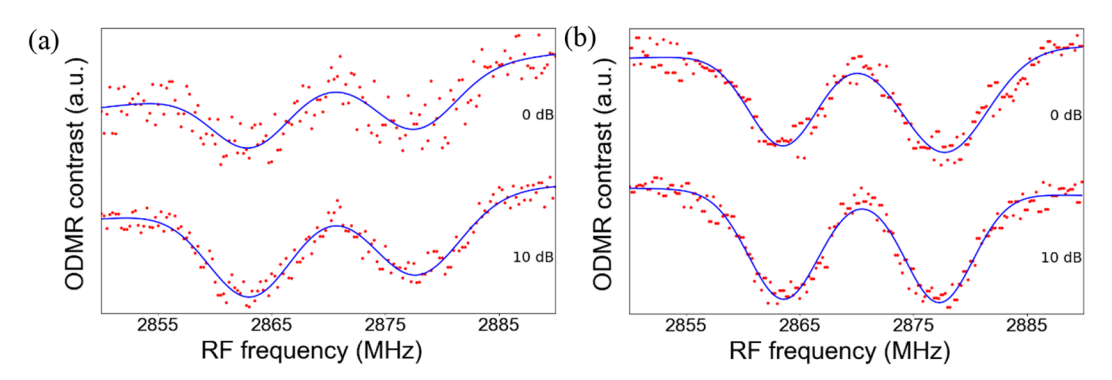


FIG. 4. ODMR spectra at different input RF powers obtained with (a) single and (b) double ring RF antennas. Dots represent experimental data points and solid lines are fitted data using Lorentzian functions for the ODMR dips.

We utilized expectation-maximization (E-M) based machine learning (ML) algorithms for the precise determination and elimination of instrumental noise in the ODMR measurements. These ML algorithms ensure that the automated experiments start after the laser power stabilizes and fluctuation is below 1%. Background counts at the pixel level in our typical experiments are around 3%. Therefore, ML algorithms clean up the spectra by eliminating the noise at the beginning that results in precise data collection through the spectrometer. For two types of background counts (dark counts and substrate/contamination induced extra fluorescence), ML employs mixture models (Gaussian and/or Poisson), which learn from the acquired signal to efficiently discriminate the background and the foreground signals. Our analysis showed that estimated distribution parameters for background counts by mixture models stabilize after 100 data samples and converge very quickly. This allowed us to utilize these models at the start of each experiment without considerable delay to improve the sensitivities of measurements. More specifically, we can sense a less than 0.1% PL signal change in the ODMR experiments, which was not possible before the use of ML algorithms due to inherent noise in the experiments.

A single axis Helmholtz coil was used to apply 0.5 mT magnetic field along the defect axis in all the measurements. ODMR spectra for different input RF powers for both antennas are shown in Fig. 4. An RF amplifier was not needed due to the high efficiency of the antennas and about 1% ODMR contrast was observed with 0 dB applied RF power by the signal generator. We observed a frequency difference of about 14 MHz between the two ODMR dips with the applied 0.5 mT external magnetic field, which agrees with the gyromagnetic ratio ( $\gamma \sim \! 28$  MHz/mT) of NV defect in diamond. These results demonstrate that high efficiency RF antennas remove the need for an RF amplifier in quantum sensing experiments with solid state defects such as NV color center in diamond, which is an important step toward miniaturization of solid-state defect-based quantum sensing setups.

#### IV. CONCLUSION

We demonstrated the design, fabrication, and characterization of two different high efficiency coplanar RF antennas for quantum sensing experiments. Return losses of simulated and fabricated antennas were in good agreement. Antennas with optimized

parameters exhibited up to  $-37\,\mathrm{dB}$  return loss. We also showed resonant frequency tuning with both simulated and fabricated antennas by changing the ring size. This enabled circumventing fabrication errors and resonant frequency shifts induced by materials around the antenna. We have fabricated and tested RF antennas in ODMR magnetic field sensing experiments using NV defects in bulk diamond, where 0 dB output of a standard RF signal generator was adequate, and an RF amplifier was not needed. This work constitutes a milestone toward the realization of field portable quantum magnetometers, which are yet to bedemonstrated.

#### SUPPLEMENTARY MATERIAL

See the supplementary material for Explanation and diagram of the custom built confocal photoluminescence setup.

#### **ACKNOWLEDGMENTS**

This material is based on work supported by the National Science Foundation under Grant Nos. 1831954 and 2101102, the Air Force Office of Scientific Research under Grant No. FA9550-19-1-0122. We gratefully acknowledge the funding support from the Department of Energy/National Nuclear Security Agency (Grant No. DE-FOA-0003945).

#### **AUTHOR DECLARATIONS**

#### **Conflict of Interest**

The authors have no conflicts to disclose.

#### **Author Contributions**

S. Mahtab: Data curation (lead); Formal analysis (supporting); Methodology (supporting); Writing – original draft (lead); Writing – review & editing (supporting). P. Milas: Conceptualization (equal); Data curation (equal); Formal analysis (equal); Investigation (equal); Methodology (equal); Software (equal). D.-T. Veal: Data curation (supporting); Software (supporting); Visualization (supporting). M. G. Spencer: Conceptualization (supporting); Funding acquisition (supporting); Investigation (supporting); Resources (supporting). B. Ozturk: Conceptualization (lead); Data curation (supporting); Formal analysis (lead); Funding acquisition (lead); Investigation (lead); Methodology (lead); Project administration (lead); Resources (lead); Software (supporting); Supervision (lead); Validation (lead); Visualization (supporting); Writing – original draft (supporting); Writing – review & editing (lead).

#### **DATA AVAILABILITY**

The data that support the findings of this study are available from the corresponding author upon reasonable request.

#### **REFERENCES**

<sup>1</sup>J. Preskill, "Quantum computing in the NISQ era and beyond," Quantum **2**, 79 (2018)

- <sup>2</sup>National Academies of Sciences, Engineering, and Medicine, *Quantum Computing: Progress and Prospects* (The National Academies Press, 2019).
- <sup>3</sup>D. Cozzolino, B. Da Lio, D. Bacco, and L. K. Oxenløwe, "High-dimensional quantum communication: Benefits, progress, and future challenges," Adv. Quantum Technol. **2**(12), 1900038 (2019).
- <sup>4</sup>C. L. Degen, F. Reinhard, and P. Cappellaro, "Quantum sensing," Rev. Mod. Phys. 89(3), 035002 (2017).
- <sup>5</sup>G. Zhang, Y. Cheng, J.-P. Chou, and A. Gali, "Material platforms for defect qubits and single-photon emitters," Appl. Phys. Rev. 7(3), 031308 (2020).
- <sup>6</sup>J. M. Taylor, P. cappellaro, L. childress, L. Jiang, D. Budker, P. R. Hemmer, A. Yacoby, R. Walsworth, and M. D. Lukin, "High-sensitivity diamond magnetometer with nanoscale resolution," Nat. Phys. 4(10), 810–816 (2008).
- <sup>7</sup>Z. Qiu, A. Hamo, U. Vool, T. X. Zhou, and A. Yacoby, "Nanoscale electric field imaging with an ambient scanning quantum sensor microscope," npj Quantum Inf. 8(1), 107 (2022).
- <sup>8</sup>S. Sotoma, C. Zhong, J. C. Y. Kah, H. Yamashita, T. Plakhotnik, Y. Harada, and M. Suzuki, "In situ measurements of intracellular thermal conductivity using heater-thermometer hybrid diamond nanosensors," Sci. Adv. 7(3), eabd7888 (2021).
- <sup>9</sup>G. Balasubramanian, P. Neumann, D. Twitchen, M. Markham, R. Kolesov, N. Mizuochi, J. Isoya, J. Achard, J. Beck, J. Tissler, V. Jacques, P. R. Hemmer, F. Jelezko, and J. Wrachtrup, Nat. Mater. **8**, 383 (2009).
- <sup>10</sup>B. Pingault, D.-D. Jarausch, C. Hepp, L. Klintberg, J. N. Becker, M. Markham, C. Becher, and M. Atatüre, "Coherent control of the silicon-vacancy spin in diamond," Nat. Commun. 8(1), 15579 (2017).
- <sup>11</sup>P.-C. Tsai, O. Y. Chen, Y.-K. Tzeng, Y. Y. Hui, J. Y. Guo, C.-C. Wu, M.-S. Chang, and H.-C. Chang, "Gold/diamond nanohybrids for quantum sensing applications," EPJ Quantum Technol. **2**(1), 1–12 (2015).
- <sup>12</sup>K. Sasaki, Y. Monnai, S. Saijo, R. Fujita, H. Watanabe, J. Ishi-Hayase, K. M. Itoh, and E. Abe, "Broadband, large-area microwave antenna for optically detected magnetic resonance of nitrogen-vacancy centers in diamond," Rev. Sci. Instrum. 87(5), 053904 (2016).
- <sup>13</sup> X. Yang, N. Zhang, H. Yuan, G. Bian, P. Fan, and M. Li, "Microstrip-line resonator with broadband, circularly polarized, uniform microwave field for nitrogen vacancy center ensembles in diamond," AIP Adv. 9(7), 075213 (2019).
- <sup>14</sup>K. Bayat, J. Choy, M. Farrokh Baroughi, S. Meesala, and M. Loncar, "Efficient, uniform, and large area microwave magnetic coupling to NV centers in diamond using double split-ring resonators," Nano Lett. 14(3), 1208–1213 (2014).
- <sup>15</sup>L. Qin, Y. Fu, S. Zhang, J. Zhao, J. Gao, H. Yuan, Z. Ma, Y. Shi, and J. Liu, "Near-field microwave radiation function on spin assembly of nitrogen vacancy centers in diamond with copper wire and ring microstrip antennas," Jpn. J. Appl. Phys. 57(7), 072201 (2018).
- <sup>16</sup>G. Singla and R. Khanna, "Double-ring multiband microstrip patch antenna with parasitic strip structure for heterogeneous wireless communication systems," Int. J. Microwave Wireless Technol. 9(8), 1757–1762 (2017).
- <sup>17</sup>J.-S. Chen, "Dual-frequency annular-ring slot antennas fed by CPW feed and microstrip line feed," IEEE Trans. Antennas Propag. 53(1), 569–573 (2005).
- <sup>18</sup> J. Anguera, A. Andujar, and C. Garcia, "Multiband and small coplanar antenna system for wireless handheld devices," IEEE Trans. Antennas Propag. 61(7), 3782–3789 (2013).
- <sup>19</sup>T. Jang, J. Choi, and S. Lim, "Compact coplanar waveguide (CPW)-fed zeroth-order resonant antennas with extended bandwidth and high efficiency on vialess single layer," IEEE Trans. Antennas Propag. 59(2), 363–372 (2010).
- <sup>20</sup> M. Zhao, Q. Lin, L. Zhu, L. Zhao, and Z. Jiang, "Antenna for microwave manipulation of NV colour centres," Micro Nano Lett. 15(12), 793–796 (2020).
- <sup>21</sup>P. Milas, S. Mathab, J. B. Sam Abraham, J. Alam, M. V. S. Chandrashekar, A. J. Robinson, P. M. Vora, B. Ozturk, and M. G. Spencer, "Electronic and optical characterization of bulk single crystals of cubic boron nitride (cBN)," AIP Adv. 12(9), 095303 (2022).
- <sup>22</sup>S. Mathab, P. Milas, Md J. Alam, M. V. S. Chandrashekhar, M. G. Spencer, and B. Ozturk, "Room temperature RC series zero phonon line emission from electron irradiated cubic boron nitride," in *Quantum 2.0* (Optica Publishing Group, 2022), pp. QTu2A-26.